

# Coulomb collisions of hot and cold single electrons in series-coupled silicon single-electron pumps

Gento Yamahata<sup>✉,\*</sup>, Nathan Johnson,<sup>†</sup> and Akira Fujiwara

*NTT Basic Research Laboratories, NTT Corporation, 3-1 Morinosato Wakamiya, Atsugi, Kanagawa 243-0198, Japan*

 (Received 30 March 2023; revised 26 July 2023; accepted 26 September 2023; published 17 October 2023)

Precise understanding of the Coulomb interaction between single electrons is vital to achieve accurate single-electron control toward quantum current standards and quantum information processing. Since the strength of the Coulomb interaction increases with decreasing distance, a collision experiment of single electrons would be an ideal way to investigate it. It would be useful to study such a Coulomb collision in silicon single-electron pumps, which can accurately transfer single electrons one by one, while silicon systems have not been used for making Coulomb collisions at the single-electron level. Here, we made two series-coupled tunable-barrier single-electron pumps in silicon and used one to inject a hot single electron into the other pump in each pumping cycle. The hot single electron collides with a cold single electron confined in the other single-electron pump. We observed a current flow due to ejection not only of the hot single electron but also of the confined cold single electron. The latter leads to an excess current at a current plateau at a certain voltage range. We also found that increasing the number of cold electrons from one to two increased the cold-electron current by at least twofold. These results can be explained by a charging effect due to the Coulomb interaction. This observation is valuable to understand single-electron dynamics in the silicon single-electron devices toward accurate current generation and quantum manipulation of flying single electrons.

DOI: [10.1103/PhysRevApplied.20.044043](https://doi.org/10.1103/PhysRevApplied.20.044043)

## I. INTRODUCTION

A single-electron (SE) pump using a clock-controlled dynamic quantum dot (QD) can accurately emit hot electrons one by one [1]. It can be used for applications to quantum current standards [2,3], quantum information technology [4,5], quantum sensing [6], and electron quantum optics [7,8]. An attractive device toward these goals is a silicon tunable-barrier SE pump, as it is capable of high-accuracy and high-speed operation [9,10] even at a liquid helium temperature [11]. However, there is still a need for investigating device reproducibility in terms of the pumping error rate [12]. One worthwhile point to understand in depth would be the Coulomb interaction between SEs. While the dynamics of the SE pumping can be simply modeled using master equations [13,14], detailed understanding of the microscopic interaction in a dynamic QD is helpful to fully understand the pumping accuracy.

Another motivation for investigating the Coulomb interaction is related to quantum information processing using flying SEs [15]. This type of flying qubit has recently

attracted attention [16–19] as a counterpart of photonic quantum computing [20,21] because, as opposed to photons, SEs inherently have the Coulomb interaction, with which a deterministic two-qubit gate is expected to be realized [22]. Recently, the unscreened Coulomb interaction has been experimentally observed between two flying SEs generated by GaAs SE pumps [23,24] and by surface acoustic waves in a GaAs device [25]. Theoretical works have also pointed out the significance of the Coulomb interaction [26–28]. These results would indicate that the unscreened devices are useful for achieving a controllable flying-qubit gate.

Considering the above background, it is valuable to investigate the Coulomb interaction of SEs in silicon. So far, there have been investigations on the Coulomb interaction between a hot electron and many electrons in the Fermi sea of silicon devices [29,30] and amplification of current due to the Coulomb interaction has been reported [30]. However, there is no report on the Coulomb interaction of hot electrons at the SE level. Here, we propose to use two SE pumps based on silicon QDs that are connected in series for collision experiments between a hot flying SE and a cold SE trapped in one of the QDs. We observe an excess current at the current plateau of the series-coupled SE pumps that is evidence of the unscreened Coulomb interaction.

\*gento.yamahata@ntt.com

<sup>†</sup>Present Address: London Centre for Nanotechnology, University College London, London WC1H 0AH, United Kingdom.

The outline of this paper is as follows. We introduce the device structure, its fabrication process, and the measurement scheme of the SE-collision experiments in Sec. II. Then, we describe and discuss the experimental results in Sec. III. In particular, Sec. III A discusses the current transport characteristics of the individual SE pumps and shows that each pump operated accurately. In Sec. III B, we demonstrate a detection of hot SEs injected from one SE pump by a detection barrier. Section III C describes injection of a hot SE pumped from one SE pump into a neighboring one-electron QD, and an experimentally observed increase in current originating from the cold SE trapped in the QD due to the Coulomb interaction. Section III D explores injection of a hot SE pumped from one SE pump into a neighboring two-electron QD, for which the experimental results were consistent with the one-electron case. Section III E is an additional discussion. Section IV is the conclusion.

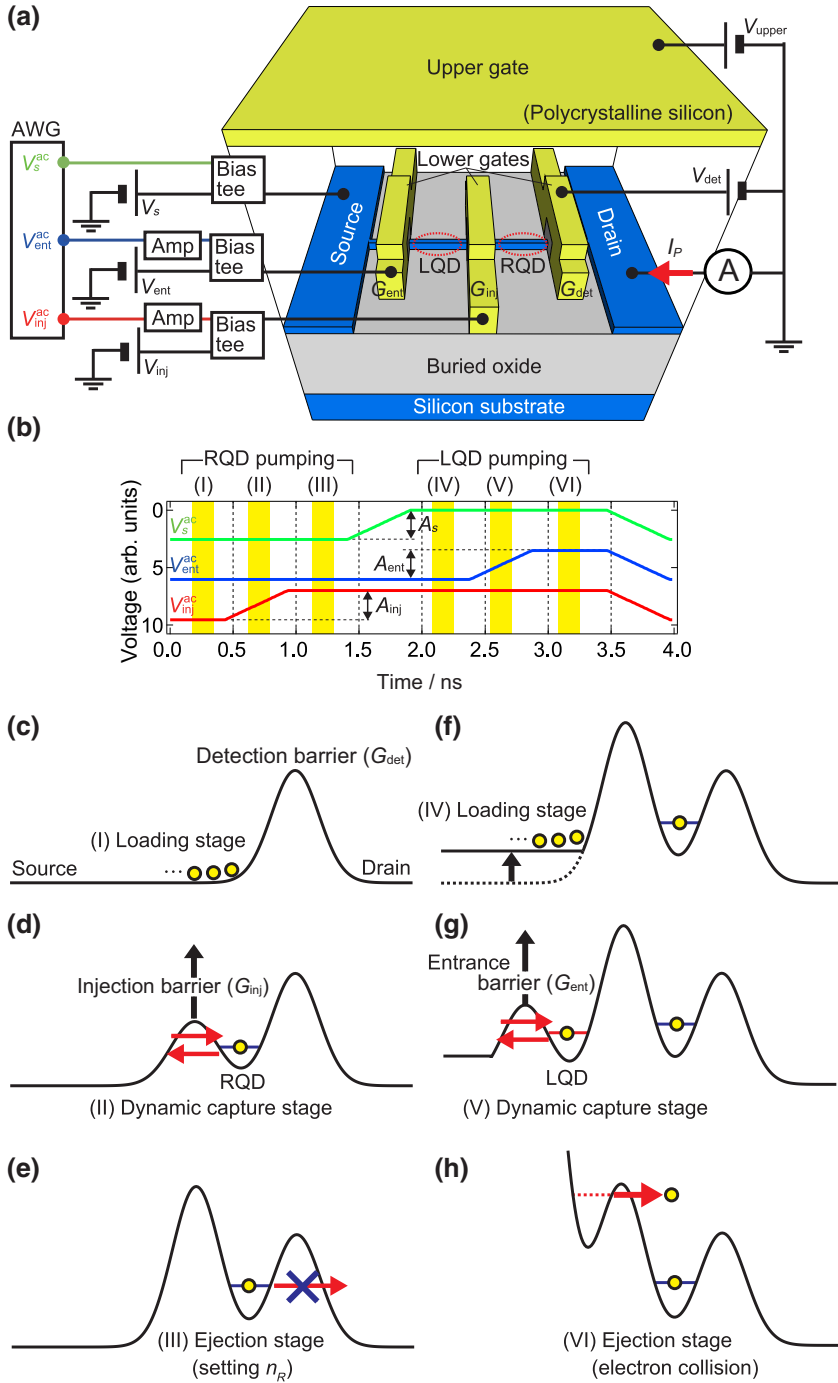
## II. DEVICE AND MEASUREMENT SCHEME

Figure 1(a) shows the schematic device structure together with the electrical connections [5,9,31]. The fabrication process is as follows. A nondoped silicon wire is formed on 400-nm-thick buried oxide by using electron-beam lithography and dry etching, followed by thermal oxidation for forming 30-nm-thick silicon dioxide. Next, *n*-type polycrystalline silicon is grown by chemical vapor deposition. This layer is patterned using electron-beam lithography and dry etching to form the three lower gates ( $G_{\text{ent}}$ ,  $G_{\text{inj}}$ ,  $G_{\text{det}}$ ) on the silicon wire. After growth of inter-layer silicon dioxide to a thickness of 50 nm by chemical vapor deposition, *n*-type polycrystalline silicon is again grown by chemical vapor deposition. This layer is patterned using optical lithography and dry etching to form an upper gate covering the whole region of the silicon wire. Then, the upper gate is used as a mask for ion implantation to form *n*-type source and drain electrodes. Finally, aluminum Ohmic contacts to the source, drain, and gate electrodes are formed using vacuum deposition. The diameter of the silicon wire, lower gate lengths, and spacing between adjacent lower gates are 15, 10, and 100 nm, respectively.

The device was cooled in a dilution refrigerator at a base temperature of 20 mK unless otherwise noted. Three synchronized high-frequency voltages  $V_s^{\text{ac}}$ ,  $V_{\text{ent}}^{\text{ac}}$ , and  $V_{\text{inj}}^{\text{ac}}$  with amplitudes of  $A_s$ ,  $A_{\text{ent}}$ , and  $A_{\text{inj}}$  generated by an arbitrary waveform generator and dc offset voltages  $V_s$ ,  $V_{\text{ent}}$ , and  $V_{\text{inj}}$  were applied to the source,  $G_{\text{ent}}$ , and  $G_{\text{inj}}$ , respectively. The voltage pulse scheme is shown in Fig. 1(b), where the positive direction of the vertical axis is set downward to match the movement of the potential barriers shown later. In addition, dc voltages  $V_{\text{det}}$  and  $V_{\text{upper}}$  were applied to  $G_{\text{det}}$  and the upper gate, respectively.

Application of a positive dc voltage to the upper gate ( $V_{\text{upper}} = 1.2$  V) induces electrons in the source and drain electrodes. The three lower gates electrostatically define the QDs used in this work. When sufficiently large negative voltages were applied to  $G_{\text{ent}}$ ,  $G_{\text{inj}}$ , and  $G_{\text{det}}$ , a tunnel barrier was formed in the silicon wire under each gate. They are referred to as entrance, injection, and detection barriers, respectively [see Figs. 1(c), 1(d), and 1(g)]. To perform the SE collision experiments in the electron pumping regime, we perform tunable-barrier SE pumping [1,13,14] using the right QD (RQD) between  $G_{\text{inj}}$  and  $G_{\text{det}}$  in the first step [periods I–III in Fig. 1(b)] and then using the left QD (LQD) between  $G_{\text{ent}}$  and  $G_{\text{inj}}$  in the second step [periods IV–VI in Fig. 1(b)]. The source voltages for the RQD and LQD pump are changed to adjust the number of SEs captured by each QD. At period I,  $V_s^{\text{ac}}$ ,  $V_{\text{ent}}^{\text{ac}}$ , and  $V_{\text{inj}}^{\text{ac}}$  were set to their maximum amplitudes  $A_s$ ,  $A_{\text{ent}}$ , and  $A_{\text{inj}}$  respectively. In addition, a large negative  $V_{\text{det}}$  was applied to  $G_{\text{det}}$  to form a detection barrier in the silicon wire under  $G_{\text{det}}$ . This barrier prevents electron transport directly from the source to drain over the detection barrier, which is confirmed by observation of accurate SE pumping current (see later) without additional current. In this period, some electrons are loaded from the source into the region where the RQD can be formed [loading stage: Fig. 1(c)]. Then, the injection barrier rises at period II. At the same time, the RQD potential also rises because of capacitive coupling between  $G_{\text{inj}}$  and the RQD [Fig. 1(d)]. In this period, some electrons escape back to the source and an SE can be captured by the RQD during the rise of the injection barrier. Since this is a dynamic process, we call this period the dynamic capture stage. After that, the SE captured by the RQD can be ejected to the drain over the detection barrier (ejection stage). For the purpose of the collision experiment, we need to keep the SE in the RQD, which can be achieved by setting the detection barrier sufficiently high relative to the RQD [Fig. 1(e)]. The number ( $n_R$ ) of SEs in the RQD can be reset in each cycle, which is necessary because subsequent injection of an SE from the LQD might increase  $n_R$ . Then, the source voltage changes for the LQD pump toward period IV [Fig. 1(f)]. This period corresponds to the loading stage for the LQD pumping. Period V corresponds to the dynamic capture stage for the LQD pump similar to that for the RQD [Fig. 1(g)]. Here, an SE is dynamically captured by the LQD during rise of the entrance barrier. Finally, a hot SE is injected from the LQD into the RQD at period VI [Fig. 1(h)], which is an ejection stage of the LQD. The energy of the hot SE is controlled by  $V_{\text{inj}}$ . In this final situation, the hot SE injected from the LQD can be collided with the cold SE confined in the RQD for investigation of the Coulomb interaction. Note that the two QDs are independently operated throughout the process.

The dc current ( $I_P$ ) flowing through the silicon wire was measured at the drain terminal during the above



series-coupled SE pumping operation. The frequency  $f$  of the signals was 250 MHz for all SE pumping measurements. For  $n$  electrons transferred in a cycle,  $I_P = nef \sim 40 \times n$  pA, where  $e$  is the elementary charge. Note that  $V_s$  was only used for the dc transport measurements ( $V_s = 0$  V for the SE pumping). In the next section, we will break down this electron transfer process into several substages in order to analyze the electron collision.

FIG. 1. (a) Schematic device structure. The left (right) quantum dot [LQD (RQD)] is formed between  $G_{\text{ent}}$  ( $G_{\text{det}}$ ) and  $G_{\text{inj}}$ . The upper gate covers the whole region of the silicon wire and a part of the source and drain regions. dc voltages are applied to the upper gate ( $V_{\text{upper}}$ ) and  $G_{\text{det}}$  ( $V_{\text{det}}$ ). High-frequency signals generated by an arbitrary waveform generator (AWG; Keysight M8195A) combined with dc voltages using bias tees are applied to the source electrode ( $V_s^{\text{ac}} + V_s$ ),  $G_{\text{ent}}$  ( $V_{\text{ent}}^{\text{ac}} + V_{\text{ent}}$ ), and  $G_{\text{inj}}$  ( $V_{\text{inj}}^{\text{ac}} + V_{\text{inj}}$ ).  $V_{\text{ent}}^{\text{ac}}$  and  $V_{\text{inj}}^{\text{ac}}$  are amplified by a 15-GHz low-noise amplifier (Tektronix PSPL8003) with a nominal gain of 15 dB. A  $-2$ -dB attenuator is connected after the bias tee for  $V_{\text{inj}}^{\text{ac}}$  and  $-3$ -dB attenuators are set before the bias tee for  $V_s^{\text{ac}}$  and  $V_{\text{ent}}^{\text{ac}}$  (not shown). All dc voltages are supplied by dc voltage sources (Yokogawa GS200). The dc current  $I_P$  at the drain terminal is converted into a dc voltage using a programmable current amplifier (NF CA5351) and the output dc voltage is measured using a digital multimeter (Keysight 3458A). (b) Pulse sequence for the collision measurement.  $A_s$ ,  $A_{\text{ent}}$ , and  $A_{\text{inj}}$  are the amplitudes of  $V_s^{\text{ac}}$ ,  $V_{\text{ent}}^{\text{ac}}$ , and  $V_{\text{inj}}^{\text{ac}}$ , respectively (output impedance is 50  $\Omega$ ). The frequency  $f$  is 250 MHz. All rise and fall times are 0.5 ns. (c)–(h) Schematic potential diagrams during a collision measurement. The diagrams with I, II, III, IV, V, and VI correspond to those denoted in (b), respectively. The yellow dots are single electrons. The number of electrons in the RQD is initialized to one in this case (c)–(e). An SE from the source electrode is captured by the LQD (f)–(g) and eventually injected into the RQD as a hot SE (h).

### III. EXPERIMENTAL RESULTS AND DISCUSSIONS

#### A. Individual SE pump characteristics

First, the individual SE pump characteristics were checked using only the LQD or only the RQD as single QDs. To transfer SEs using the LQD (RQD), we applied a positive dc voltage to  $G_{\text{det}}$  ( $G_{\text{ent}}$ ) to sufficiently lower

the detection (entrance) barrier. Then, we applied a high-frequency signal only to  $G_{\text{ent}}$  ( $G_{\text{inj}}$ ) for the LQD (RQD) pump. The pulse shape was identical to that shown in Fig. 1(b).

Figure 2(a) shows  $I_P$  as a function of  $V_{\text{ent}}$  and  $V_{\text{inj}}$  when only the LQD pump was operated. The left, bottom, and right boundaries of the trapezoidal current-generating

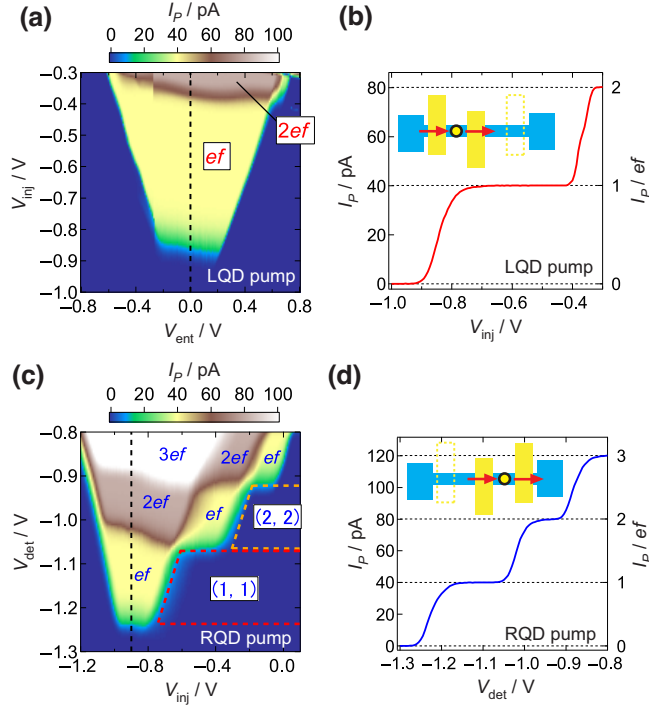


FIG. 2. (a) Current  $I_P$  as a function of  $V_{\text{ent}}$  and  $V_{\text{inj}}$  at  $f = 250$  MHz, where  $V_{\text{upper}} = 1.2$  V,  $V_{\text{det}} = 1$  V, and  $V_s = 0$  V. The high-frequency signal with an amplitude  $A_{\text{ent}} = 0.3$  V (nominal amplitude of 2.4 V at the gate electrode obtained taking into account the gain of the amplifier and the attenuation of the attenuator) is applied to  $G_{\text{ent}}$ . Note that this amplitude was selected to prevent breakdown of the device (safe range for our devices). (b)  $I_P$  (left axis) and  $I_P/ef$  (right axis) as a function of  $V_{\text{inj}}$  at  $f = 250$  MHz, where  $V_{\text{upper}} = 1.2$  V,  $V_{\text{det}} = 1$  V,  $V_{\text{ent}} = 0$  V,  $V_s = 0$  V, and  $A_{\text{ent}} = 0.3$  V, corresponding to the black dashed line in (a). The inset is a schematic diagram of the LQD pump. (c)  $I_P$  as a function of  $V_{\text{inj}}$  and  $V_{\text{det}}$  at  $f = 250$  MHz, where  $V_{\text{upper}} = 1.2$  V,  $V_{\text{ent}} = 1$  V, and  $V_s = 0$  V. The high-frequency signal with an amplitude  $A_{\text{inj}} = 0.3$  V (nominal amplitude of 2.7 V at the gate electrode obtained taking into account the gain of the amplifier and the attenuation of the attenuator) is applied to  $G_{\text{inj}}$ . The areas within the red dashed lines are the values of  $V_{\text{inj}}$  and  $V_{\text{det}}$  at which one electron is dynamically captured and it remains in the RQD [denoted as (1, 1) in this region], when the height of the injection barrier is at its maximum (see Appendix A) [3]. Similarly, the areas within the orange dashed lines is assigned as (2, 2). (d)  $I_P$  (left axis) and  $I_P/ef$  (right axis) as a function of  $V_{\text{det}}$  at  $f = 250$  MHz, where  $V_{\text{upper}} = 1.2$  V,  $V_{\text{ent}} = 1$  V,  $V_{\text{inj}} = -0.9$  V,  $V_s = 0$  V, and  $A_{\text{inj}} = 0.3$  V, corresponding to the black dashed line in (c). The inset is a schematic diagram of the RQD pump.

region correspond to loading, dynamic capture, and ejection of SEs, respectively [1,3] (see Appendix A for further discussion). The current along the black dashed line on the LQD pump map at  $V_{\text{ent}} = 0$  in Fig. 2(a) has a clear current plateau with a level of  $ef$  [Fig. 2(b)]. This indicates that a dynamically captured SE is accurately ejected to the drain. This accurate ejection is helpful to achieve the final condition for the collision experiment shown in Fig. 1(h).

Figure 2(c) shows  $I_P$  as a function of  $V_{\text{inj}}$  and  $V_{\text{det}}$  when only the RQD pump was operated. The current along the black dashed line on the RQD pump at  $V_{\text{inj}} = -0.9$  V in Fig. 2(c) has clear plateaus with levels of  $ef$  and  $2ef$  [Fig. 2(d)]. This indicates that one or two SEs are dynamically captured and eventually ejected to the drain with high precision. For the collision experiments, it is necessary that SEs remain captured by the RQD. Setting voltages to values inside the red (orange) dashed line in Fig. 2(c) allows one to capture one (two) SE(s) in the dynamic capture stage but not to eject the SE(s) to the drain in the ejection stage because of the high detection barrier (see also Appendix A). We focused on these regions in the following measurements.

## B. Detection of hot SEs injected from the LQD

We investigate injection of a hot SE from the LQD into the RQD without loading electrons from the source to the RQD at the loading stage [Fig. 1(c)], which was achieved by following the pulse sequence given in Fig. 1(b) and minimizing  $A_{\text{inj}}$ . In this case, all SEs ejected to the drain across the RQD and the detection barrier are pumped by the LQD. When the energy of the hot SE injected from the LQD is lower than the height of the detection barrier, which is tuned by  $V_{\text{det}}$ , the hot SE cannot be ejected to the drain [see Fig. 1(h)]. This suppresses  $I_P$ , and the energy of the hot SE injected from the LQD with respect to the detection barrier top can be estimated.

Figure 3(a) shows  $I_P$  as a function of  $V_{\text{inj}}$  and  $V_{\text{det}}$  under the above conditions. The three vertical lines in solid red indicate threshold voltages for the dynamic capture stage of the LQD during the rise of the entrance barrier. This is confirmed by the LQD pump map in this case as shown in Fig. 3(b). A dashed horizontal line in Fig. 3(a) corresponds to a dashed vertical line in Fig. 3(b). The red line rising to the right in Fig. 3(a) indicates the threshold voltage for the hot SE injected from the LQD to be blocked by the detection barrier. This threshold is determined by the injection barrier height (i.e., injection energy) and the detection barrier height, which are controlled mainly by  $V_{\text{inj}}$  and  $V_{\text{det}}$ , respectively. Since the voltage-to-energy conversion factors of these two modulations are almost the same (Appendix B), the slope of the threshold line is almost unity.

The red line in Fig. 3(c) corresponds to the vertical black dashed line on the pump map in Fig. 3(a). The current

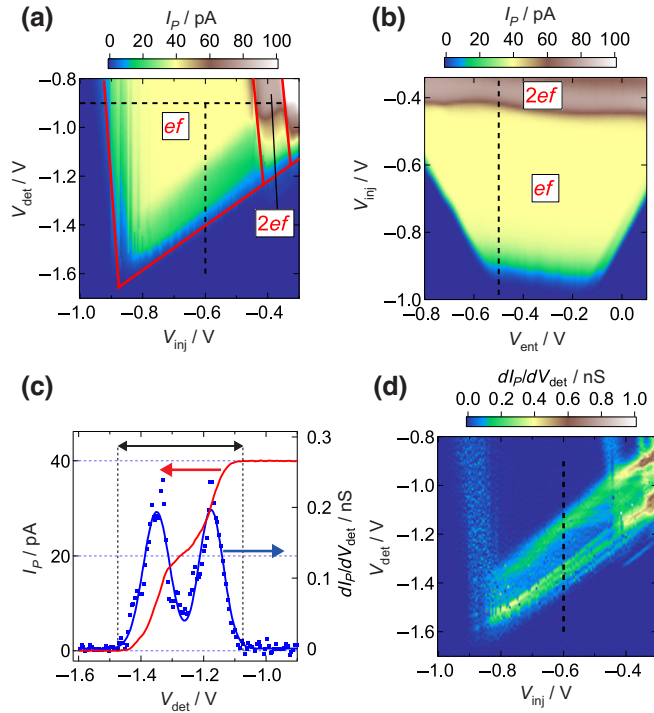


FIG. 3. (a)  $I_p$  as a function of  $V_{inj}$  and  $V_{det}$  with the pulse sequence shown in Fig. 1(b), where  $V_{upper} = 1.2$  V,  $V_{ent} = -0.5$  V,  $V_s = 0$  V,  $A_{ent} = 0.3$  V,  $A_{inj} = 0.075$  V, and  $A_s = 0.5$  V. (b)  $I_p$  as a function of  $V_{ent}$  and  $V_{inj}$  with the pulse sequence shown in Fig. 1(b), where  $V_{upper} = 1.2$  V,  $V_{det} = -0.9$  V,  $V_s = 0$  V,  $A_{ent} = 0.3$  V,  $A_{inj} = 0.075$  V, and  $A_s = 0.5$  V. The vertical black dashed line corresponds to the horizontal black dashed line in (a). (c)  $I_p$  (red line; left axis) and  $dI_p/dV_{det}$  (blue dots; right axis) as a function of  $V_{det}$ , which corresponds to the vertical black dashed lines in (a) and (d), respectively, where  $V_{inj} = -0.6$  V. The fit (blue line) to the blue dots is composed of two Gaussian functions:  $A\exp[-\{(V_{det} - V_1)/w_1\}^2] + B\exp[-\{(V_{det} - V_2)/w_2\}^2]$ , where  $V_1$ ,  $V_2$ ,  $w_1$ ,  $w_2$ ,  $A$ , and  $B$  are constants.  $\Delta V_{det} = V_2 - V_1 \sim 0.17$  V. (d) The first derivative of  $I_p$  shown in (a).

plateau is at the level of  $ef \sim 40$  pA at around  $V_{det} = -1$  V. This indicates that the hot SE injected from the LQD was ejected to the drain in every cycle. In addition, there is a clear two-step feature in  $I_p$ . To examine it, we differentiated  $I_p$  with respect to  $V_{det}$  [blue dots in Fig. 3(c)]. A fit to the  $dI_p/dV_{det}$  data in Fig. 3(c) using two Gaussian functions roughly reveals the spacing of these two peaks,  $\Delta V_{det} \sim 0.17$  V.

To convert  $V_{det}$  into a hot-SE energy relative to the top of the detection barrier, we estimated the voltage-to-energy conversion factors between  $G_{det}$  and the detection barrier ( $\alpha_{detB} = 0.40$  eV/V) and between  $G_{det}$  and the injection barrier ( $\alpha_{det-injB} \sim 0.034$  eV/V) from dc measurements (Appendix B). The latter estimate is necessary because the energy of the hot SE injected from the LQD is determined by the height of the injection barrier. Here, the minimum energy scale required for the ejection of the hot SE injected from the LQD to the drain in every cycle

roughly corresponds to the length of the black arrow in Fig. 3(c), which is about 0.4 V. This value is converted into an energy of  $0.4$  V  $\times$  ( $\alpha_{detB} - \alpha_{det-injB}$ )  $\sim 0.15$  eV and is considered to be a typical energy of a hot SE injected from the LQD in this experiment. Then, the spacing  $\Delta V_{det}$  was converted into an energy:  $\Delta V_{det} \times (\alpha_{detB} - \alpha_{det-injB}) \sim 62$  meV.

The lines of peaks on the pump map are parallel with an energy difference of about 62 meV [Fig. 3(d)]. Such parallel peak structures have been reported in hot-electron injection experiments on GaAs devices with quantum point contacts [32] and SE pumps [33,34], in which the spacing is understood to be a result of relaxation of an electron due to LO-phonon emission with an energy of 36 meV. On the other hand, previous hot-electron injection experiments in silicon devices have not revealed evidence of phonon relaxation [29,30] probably because relaxation due to the Coulomb interaction between a hot electron and many electrons in the Fermi sea is much faster than phonon relaxation. In the case of silicon, which is a nonpolar semiconductor with multiple conduction-band valleys, intervalley phonon scattering plays a significant role [35]. The largest contribution would be from what is called a g-LO phonon with an energy of 61–63 meV [35–37], which is consistent with our calculated spacing. Although the two observed peaks might originate from the g-LO phonon emission, we need to conduct further experiments on several different devices for checking reproducibility of these lines before we can make this conclusion.

### C. Hot-SE injection into a one-electron RQD

Next, we examined injection of a hot SE from the LQD into the RQD with one electron in it. Figure 4(a) shows  $I_p$  for such a case as a function of  $V_{inj}$  and  $V_{det}$ . The essential change in voltage conditions from those in Fig. 3(a) is to increase  $A_{inj}$  to capture an SE in the RQD. The  $ef$  and  $2ef$  plateaus in the left side on the map correspond to only the RQD-pump current. At the voltage conditions inside the red dashed lines, there is one electron in the RQD after the injection barrier height is raised [Fig. 1(e)]. Additionally, a hot SE is injected from the LQD into the RQD at a later time [Fig. 1(h)] at the region inside the solid red lines; it passes the detection barrier, resulting in a current. In the area within both the red lines and the red dashed lines, the hot SE injected from the LQD can collide with the SE confined in the RQD. A more detailed discussion about this complicated pump map including connection among different conditions and validation of the number of the SEs in the RQD is described in Appendix C.

To investigate this area in more detail, Figs. 4(b) and 4(c) plot  $I_p$  along the horizontal and tilted black dashed lines in Fig. 4(a). The tilted voltage line is called  $V_{tilt}$ , which is parallel to the threshold line determined by ejection of the SE from the RQD to the drain [the left red

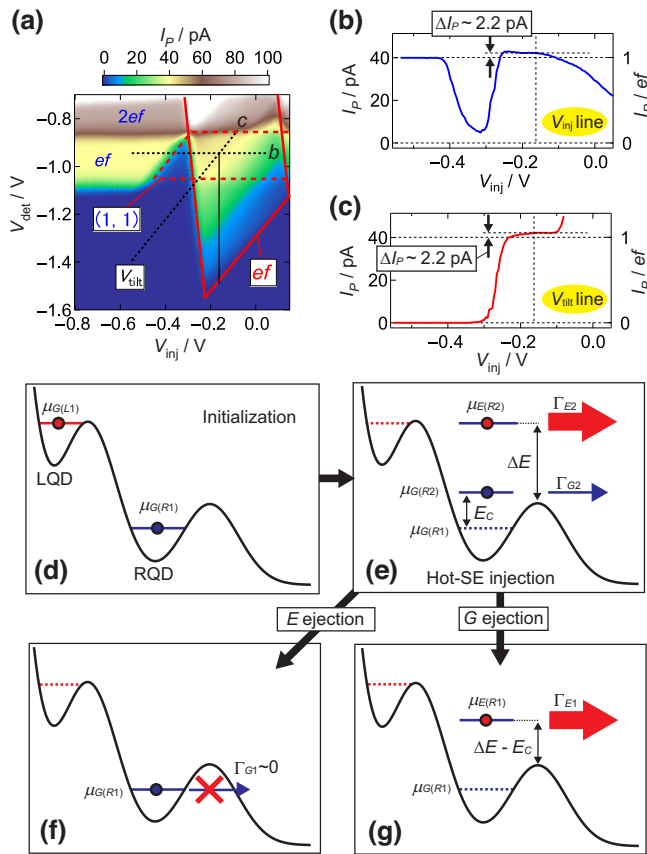


FIG. 4. (a)  $I_p$  as a function of  $V_{inj}$  and  $V_{det}$  with the pulse sequence shown in Fig. 1(b), where  $V_{upper} = 1.2$  V,  $V_{ent} = -0.5$  V,  $V_s = 0$  V,  $A_{ent} = 0.3$  V,  $A_{inj} = 0.3$  V, and  $A_s = 0.3$  V. The slope of  $V_{tilt}$  is 1.16. The labels  $b$  and  $c$  indicate the measured points plotted in (b),(c), respectively. (b)  $I_p$  as a function of  $V_{inj}$  with the same voltage condition as (a) except  $V_{det} = -0.945$  V, corresponding to the horizontal black dashed line in (a). (c)  $I_p$  as a function of  $V_{inj}$  with the same voltage condition as (a) except  $V_{det} = 1.16V_{inj} - 0.757$  V, corresponding to the tilted black dashed line in (a). (d)–(g) Potential diagrams for the hot-SE injection into the one-electron RQD. The conduction-band bottom is fixed for simplicity.

dashed line in Fig. 4(a)]. This means that the height of the detection barrier with respect to the RQD is almost constant along  $V_{tilt}$  and the ejection probability of the SE captured by the RQD is almost constant. Note that both  $V_{inj}$  and  $V_{det}$  change along  $V_{tilt}$  but we have used  $V_{inj}$  for the horizontal axis in Fig. 4(c). The intersection point of these two lines corresponds to the vertical dashed lines in Figs. 4(b) and 4(c). Around the intersection point, there is an excess current  $\Delta I_p \sim 2.2$  pA. The fact that  $I_p$  saturates in both plots indicates that the hot SE injected from the LQD was ejected to the drain in every cycle. Thus,  $\Delta I_p$  originates from the SE confined in the RQD being kicked out via the Coulomb interaction by the injected hot SE.

Now let us explain how the SE confined in the RQD is ejected and contributes to  $\Delta I_p$  in more detail by using

the potential diagrams shown in Figs. 4(d)–4(g). As a first approximation, we consider a single-particle picture with a constant charging energy. Just before the hot SE is injected into the RQD, the LQD and RQD each have one electron [Fig. 4(d)]. Both electrons are assumed to occupy the ground state with electrochemical potentials  $\mu_{G(L1)}$  and  $\mu_{G(R1)}$ . Note that there is a small possibility of nonadiabatic excitation, but its energy scale should be much smaller than the charging energy and energy of the hot SE injected from the LQD [5].

Then, the SE is injected from the LQD to RQD [Fig. 4(e)]. At that moment, the RQD has two electrons and the charging effect due to the Coulomb interaction should appear. Therefore, the SE initially confined in the RQD occupies a ground state with electrochemical potential  $\mu_{G(R2)}$ , which has an additional energy of about charging energy  $E_C$ , roughly estimated to be 19 meV (Appendix B). Note that the conduction-band bottom in Figs. 4(d)–4(g) is fixed for simplicity but the RQD potential bottom actually rises by  $E_C$  in Fig. 4(e). On the other hand, since the hot SE injected from the LQD has a high energy, it occupies an excited state with electrochemical potential  $\mu_{E(R2)}$  in the RQD.  $\mu_{E(R2)}$  relative to the detection barrier height at the intersection point of the black dashed lines in Fig. 4(a) is roughly estimated to be 0.2 eV [a spacing of  $V_{det}$  between the onset of the current and the intersection point indicated by a black line in Fig. 4(a) is roughly 0.55 V and  $0.55 \times (\alpha_{detB} - \alpha_{det-injB}) \sim 0.2$  eV]. Since an electron occupying the ground state can be ejected to the drain at the point of intersection (see also Appendix A), the SE is ejected not only from  $\mu_{E(R2)}$  but also from  $\mu_{G(R2)}$ .

When the hot SE injected from the LQD is ejected to the drain at a rate  $\Gamma_{E2}$  (we call this situation E ejection), the remaining electron occupies  $\mu_{G(R1)}$  and it cannot be ejected to the drain [Fig. 4(f)]. On the other hand, when the ground-state SE is ejected to the drain with a rate of  $\Gamma_{G2}$  (we call this situation G ejection), the electrochemical potential of the hot SE injected from the LQD is reduced by  $E_C$ . We denote this electrochemical potential as  $\mu_{E(R1)}$ . Since Figs. 4(b) and 4(c) show current saturation, we expect that the hot SE injected from the LQD is ejected to the drain in every cycle. Since  $\Delta E - E_C \sim 0.18$  eV ( $\Delta E \sim 0.2$  eV and  $E_C \sim 0.02$  eV from the above estimations), this expectation is reasonable considering the experimental result for the case in Fig. 3(c), where ejection in every cycle is achieved with a hot-SE energy of about 0.15 eV. Note that the number of SEs in the RQD is reset in the next RQD-pump cycle and the situation returns to that of Fig. 4(d) (see also Appendix C).

In Fig. 4(b), the current level is  $ef$  near  $V_{inj} = -0.5$  V, at which the current is dominated by the dynamic capture stage of the RQD pump. Since this fact indicates that errors during the dynamic capture stage of the RQD pumping is negligible,  $\Delta I_p$  only originates from the G ejection. From the above consideration, a current level at

the intersection point of the black dashed lines in Fig. 4(a) can be expressed as  $I_P/ef = 1 + \Gamma_{G2}/(\Gamma_{E2} + \Gamma_{G2}) = 1 + \Delta I_P/ef$ . From this equation,  $\Gamma_{G2}/\Gamma_{E2} \sim 0.06$ . This low ratio is probably due to the large energy difference of the two SEs.

Now let us examine the energy changes in the saturation regime using the estimated conversion factors from the voltage to the barrier height or to the RQD energy (see Appendix B and Table I). The voltage window in the saturation regime in Figs. 4(b) and 4(c) is roughly 50 mV. In the case of the  $V_{\text{tilt}}$  line, a 50-mV change in  $V_{\text{inj}}$  accompanies a 58-mV change in  $V_{\text{det}}$ . Therefore,  $\Delta E$  changes by  $0.058\alpha_{\text{detB}} - 0.05\alpha_{\text{injB}} \sim 3$  meV. This change is negligibly small compared with the hot-SE energy of about 0.15 eV. On the other hand, in the case of the  $V_{\text{inj}}$  line, a 50-mV change in  $V_{\text{inj}}$  leads to a change in  $\Delta E$  of  $0.05(\alpha_{\text{injB}} - \alpha_{\text{inj-detB}}) \sim 19$  meV and to a change in the barrier height relative to the RQD ground state by  $0.05(\alpha_{\text{inj-RQD}} - \alpha_{\text{inj-detB}}) \sim 3$  meV. The former value is not small but, if we subtract  $E_C$  from  $\Delta E$ , we get about 0.16 eV, which indicates the possibility that the hot SE injected from the LQD was ejected to the drain in every cycle. The latter value is much smaller than  $E_C$ . These considerations support the validity of the above model.

#### D. Hot-SE injection into a two-electron RQD

Now we examine the results of hot-SE injection from the LQD into the RQD with two electrons. To increase the number of electrons captured by the RQD, we raised the Fermi level in the source during the RQD pumping by reducing  $A_s$  [see region II in Fig. 1(b)] from the voltage conditions in Fig. 4(a) (a more detailed discussion is described in Appendix C). Figure 5(a) shows a pump map including the three-electron collision conditions as a function of  $V_{\text{inj}}$  and  $V_{\text{det}}$ . The region inside the orange dashed lines corresponds to two electrons in the RQD and the region inside the red lines corresponds to hot-SE injection from the LQD. A blue line in Fig. 5(b) and a red line in Fig. 5(c) are  $I_P$  along horizontal and tilted black dashed lines in Fig. 5(a), respectively. The current level exceeds  $ef$  by about 4.5 pA at the intersection point of the two black dashed lines in Fig. 5(a).

While such an excess current can be seen more clearly in the case of the one-electron RQD, as shown in Fig. 4(b), the excess current in this case appears in a more complicated way because the two regions of our interest overlap in a narrow space in Fig. 5(a). To analyze the excess current more qualitatively, it is necessary to subtract a direct RQD pumping current because the ejection line of the RQD pump (the left orange dashed line) is close to the intersection point. For this purpose, we suppressed the injection of the hot SE from the LQD by increasing  $V_{\text{ent}}$  to 0.5 V, which corresponds to outside of the ejection line of the LQD pump (see Appendix D). A red line in

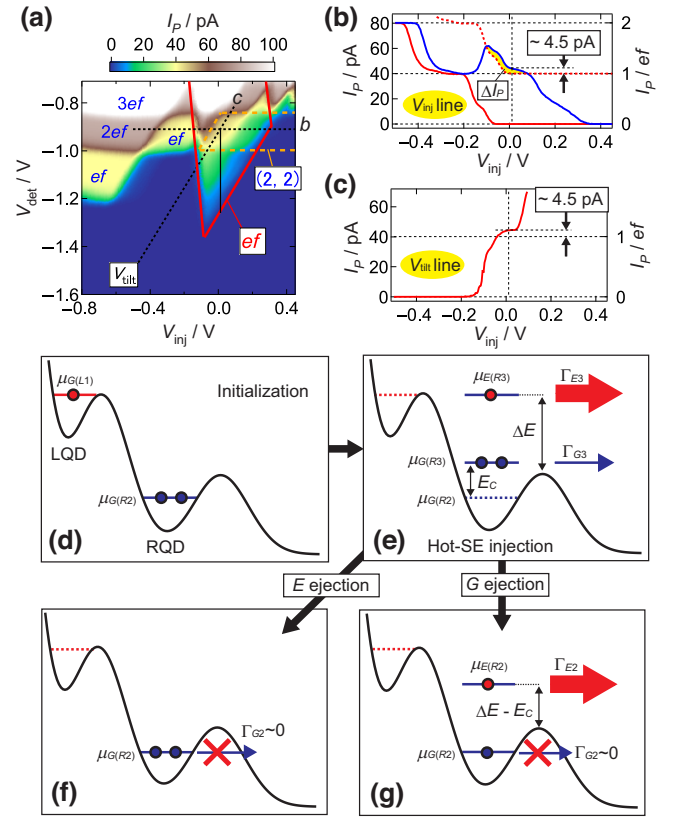


FIG. 5. (a)  $I_P$  as a function of  $V_{\text{inj}}$  and  $V_{\text{det}}$  with the pulse sequence shown in Fig. 1(b), where  $V_{\text{upper}} = 1.2$  V,  $V_{\text{ent}} = -0.3$  V,  $V_s = 0$  V,  $A_{\text{ent}} = 0.3$  V,  $A_{\text{inj}} = 0.3$  V, and  $A_s = 0.075$  V. The slope of  $V_{\text{tilt}}$  is 1.16. The labels  $b$  and  $c$  indicate the measured points plotted in (b),(c), respectively. (b) The blue line is  $I_P$  as a function of  $V_{\text{inj}}$  with the same voltage condition as (a) except  $V_{\text{det}} = -0.91$  V, corresponding to the horizontal black dashed line in (a). The red line is  $I_P$  measured using the same condition as the blue line except for  $V_{\text{ent}} = 0.5$  V. A red dashed line is a copy of the red line with a horizontal shift of 56 mV and a vertical shift of 40 pA. (c)  $I_P$  as a function of  $V_{\text{inj}}$  with the same voltage condition as (a) except  $V_{\text{det}} = 1.16V_{\text{inj}} - 0.924$  V, corresponding to the tilted black dashed line in (a). (d)–(g) Potential diagrams for the explanation about the hot-SE injection into the two-electron RQD. The conduction-band bottom is fixed for simplicity.

Fig. 5(b) is  $I_P$  with such a condition, where we observe only RQD pumping current. Since there is a cross coupling between the entrance gate and RQD, the ejection line of the RQD has a shift. The amount of the shift is a horizontal spacing of the red and blue lines at around  $V_{\text{inj}} = -0.4$  V, at which both lines show only the RQD pumping current (see also Fig. 10). A red dashed line in Fig. 5(b) is obtained by offsetting the red line horizontally by the shift and vertically by  $ef$ . This can be an expected direct RQD pumping current because the structures at around  $V_{\text{inj}} = -0.05$  V is similar between the red dashed line and blue line (see also Appendix D). Thus, we conclude that the yellow region in Fig. 5(b) is not due

to the direct RQD pumping current. Since the excess current determined by the difference between the blue and red dashed lines at  $-0.05 \text{ V} < V_{\text{inj}} < 0 \text{ V}$  is almost constant, it is the almost gate-independent excess current due to the cold SEs, which is slightly larger than 4.5 pA. On the other hand, the yellow region becomes smaller as  $V_{\text{inj}}$  increases at  $V_{\text{inj}} > 0 \text{ V}$ . Since the excess current by the cold SEs should have a weak gate dependence similar to Fig. 4(b), the hot SE injected from the LQD was not ejected in every cycle at  $V_{\text{inj}} > 0 \text{ V}$ . This is also supported by the fact that the energy of the hot SE injected from the LQD relative to the detection barrier was only about 0.13 eV at the intersection point of the black dashed lines [a spacing of  $V_{\text{det}}$  between the onset of the current and the intersection point indicated by a black line in Fig. 5(a) is roughly 0.35 V and  $0.35 \times (\alpha_{\text{detB}} - \alpha_{\text{det-injB}}) \sim 0.13 \text{ eV}$ ]. In addition, there is an excess current of 4.5 pA along  $V_{\text{tilt}}$  but its saturation is not so clear compared with that in Fig. 4(c). This result is reasonable because the ejection probability of the hot SE injected from the LQD depends on  $V_{\text{inj}}$  and  $V_{\text{det}}$  in this regime.

Figures 5(d)–5(g) show potential diagrams in the case of the two-electron RQD. Here, the conduction-band bottom is depicted as being constant for simplicity. The ground state with electrochemical potential  $\mu_{G(L1)}$  in the LQD and the ground state with electrochemical potential  $\mu_{G(R2)}$  in the RQD are initially occupied [Fig. 5(d)]. Then, as shown in Fig. 5(e), the injection of a hot SE into the RQD leads to a charging effect similar to that in Fig. 4(e). Since there are two electrons in the ground state of the three-electron RQD, the rate  $\Gamma_{G3}$  of ejection from the ground state with electrochemical potential  $\mu_{G(R3)}$  is at least 2 times higher than  $\Gamma_{G2}$  in Fig. 4(e), in which one electron occupies the ground state with  $\mu_{G(R2)}$ . This is consistent with the fact that  $\Delta I_P$  ( $> 4.5 \text{ pA}$ ) is more than twice as large as in the case of the one-electron RQD ( $\Delta I_P \sim 2.2 \text{ pA}$ ). This consistency also shows the validity of our model.

The remaining processes are essentially the same as those of the one-electron-RQD case. When the hot SE injected from the LQD is ejected to the drain at a rate  $\Gamma_{E3}$ , two electrons remain trapped in the RQD [Fig. 5(f)]. When one of the ground-state electrons is ejected to the drain at a rate  $\Gamma_{G3}$ , only remaining hot electron can be ejected to the drain [Fig. 5(g)]. Note that  $\Delta E - E_C \sim 0.11 \text{ eV}$  is insufficient for the hot SE injected from the LQD to be ejected to the drain in every cycle (0.15 eV is necessary for ejection in every cycle as discussed in Sec. III-B). Similar to Fig. 4(b), there is a  $2ef$  plateau on the left side of Fig. 5(b), indicating negligible errors of the two-SE capture in the dynamic capture stage of the RQD.

### E. Additional discussions

Above, we explained the experimental results by using a simple single-particle model, where we assumed that the

initially captured SE in the RQD occupies the ground state. However, there is a possibility of transition of the SE from the ground to excited states in the RQD during the hot-SE propagation over the RQD. This process should accompany relaxation of the injected hot SE. If it occurs, the energy distribution of the initially confined SE becomes broad and the SE might be ejected to drain after the  $E$  ejection [Figs. 4(f) and 5(f)]. However, since the slope of the RQD ejection line for the collision condition [blue line in Fig. 5(b)] is almost the same as that for the case of no collision [red line in Fig. 5(b)], we expect that the transition is not so large in this voltage regime. This is possibly because the interaction time is too short for the transition. We should note that, although the energy distribution of the injected SE can usually be used to detect the broadening, the distribution of the injected-SE energies is broad [Fig. 3(c)] and it is impossible to distinguish the intrinsic broadening from the broadening due to the relaxation process. Therefore, we cannot exclude the possibility of a transition in the voltage regime where the direct RQD pumping current is suppressed. A previous many-electron collision experiment [30] showed that such a transition frequently occurs and leads to current amplification. In that case, the number of electrons interacting with an injected hot electron is on the order of one hundred, which might be a reason for the difference between our results and those of the previous work. The transition should be further investigated in future experiments using an RQD with a different length and an injected SE with a sharper distribution.

From the viewpoint of the error mechanism of SE pumping, the above results imply that there is a possibility of excess ejection of a trapped electron during propagation of hot SEs. For example, an electron confined in a trap level around the QD could lead to an additional leakage current during SE pumping. The Coulomb interaction between an emitted hot electron and the trapped electron might potentially enhance such a leakage. It is necessary to investigate such a possibility in more detail in future works.

Regarding flying qubit applications, the charging effect is necessary to perform two-qubit gate operation [22] but transitions between energy levels must not occur. In that sense, the small transition between the energy levels in the RQD would be good characteristics. In addition, it would be valuable to roughly estimate an expected time evolution of the phase of the two SE system [25], which is  $E_C \tau / 2\hbar \sim 18\pi$ , where  $\tau \sim 4 \text{ ps}$  is the propagation time of the injected hot SE in the RQD (we roughly use the period of coherent oscillations previously extracted from the data of our SE pump [5]) and  $\hbar$  is the reduced Planck constant. Note that  $E_C/2$  is a rough estimate of the electrostatic energy. Since  $18\pi$  is too large, this rough estimate suggests that the two SEs should be farther apart. In future experiments, the design of the device should be improved for performing appropriate qubit operations. One point is that relatively high-temperature operation of silicon SE pump

[11] is good for a flying qubit initialization because cooling power in the millikelvin regime is limited, which is a general problem of most solid-state qubit systems [38,39]. In addition, the fact that silicon has weak spin-orbit and hyperfine interactions would be an advantage for stable propagation of hot SEs. Furthermore, silicon QDs have been extensively studied toward static-qubit applications, thanks to the long coherence time of electron spins confined in the QDs and the widespread availability of silicon integration technology [40–43]. Combining them with flying electrons would be another pathway toward realization of quantum information devices [44,45].

#### IV. CONCLUSION

We investigated the injection of a hot SE into a one-electron QD or a two-electron QD by using tunable-barrier series-coupled SE pumps in silicon. The hot SE injected from one QD into neighboring another QD was ejected in every cycle when it had a sufficiently high energy ( $>0.15$  eV) with respect to the detection barrier. The hot-SE energy distribution had a two-step feature possibly due to phonon emission. In the one-electron case, we observed a current in excess of  $ef$  when the hot SE is injected. This excess current is attributed to additional ejection of the cold SE trapped in the RQD due to the Coulomb interaction (charging effect). In the two-electron case, the excess current more than doubled, which can be explained by an increase in the ejection rate of the ground-state SEs. These results indicate the existence of a strong unscreened Coulomb interaction and imply a possibility of improvement of SE pumping accuracy and of building a two-qubit gate with flying electrons in silicon.

#### ACKNOWLEDGMENTS

We thank T. Shimizu and K. Nishiguchi for fruitful discussions. This work was partly supported by JSPS KAKENHI Grant No. JP18H05258.

#### APPENDIX A: SE PUMP MAP

To find operating conditions for the collision experiments, it is necessary to precisely understand a pump map for tunable-barrier SE pumping [1,3]. Figure 6 shows a schematic pump map as a function of dc voltages applied to an entrance gate ( $V_{\text{entrance}}$ ) and an exit gate ( $V_{\text{exit}}$ ) shown in the inset. Purple, black, and light-blue lines are called loading, dynamic capture, and ejection lines, corresponding to the loading [Figs. 1(c) and 1(f)], dynamic capture [Figs. 1(d) and 1(g)], and ejection [Figs. 1(e) and 1(h)] stages. In the region to the left of the purple line (hatched region), no electrons are loaded into the QD because the entrance barrier is sufficiently high. Note that the entrance barrier is not depicted in Figs. 1(c) and 1(f) because we assume a sufficiently large pulse amplitude. Increasing

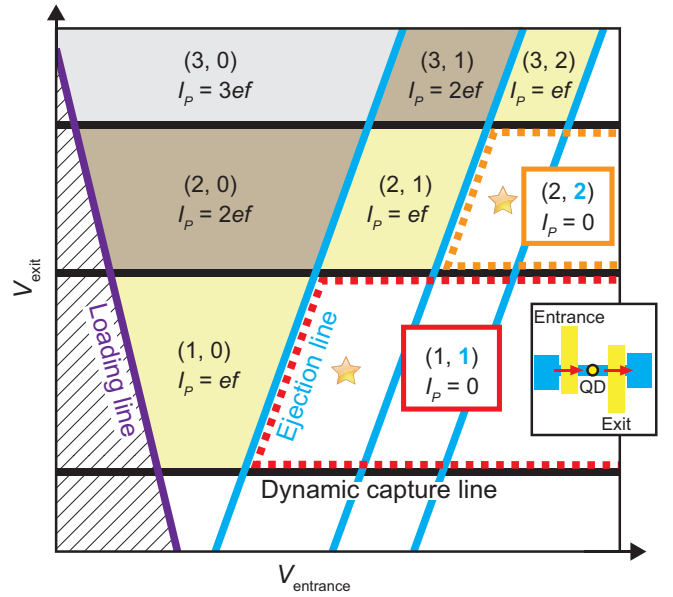


FIG. 6. Schematic diagram of an SE pump map as a function of voltages applied to an entrance gate ( $V_{\text{entrance}}$ ) and an exit gate ( $V_{\text{exit}}$ ) shown in the inset.  $(n_{\text{dc}}, n_{\text{R}})$  is denoted in each region, where  $n_{\text{dc}}$  is the number of SEs captured by the QD shown in the inset in the dynamic capture stage and  $n_{\text{R}}$  is the number of SEs captured by the QD between the ejection stage and the next loading stage. This results that  $I_P = (n_{\text{dc}} - n_{\text{R}})ef$ .

$V_{\text{exit}}$  across the bottom, middle, and top dynamic capture lines allows one, two, or three electrons to be dynamically captured during the rise of the entrance barrier. We define these numbers as  $n_{\text{dc}}$ . Increasing  $V_{\text{entrance}}$  across the left, middle, and right ejection lines, prevents one, two, or three electrons from being ejected because the exit barrier is sufficiently high. We define these numbers as  $n_{\text{R}}$ . A relevant point is that  $n_{\text{dc}} \geq n_{\text{R}}$  at a fixed  $V_{\text{exit}}$ .  $(n_{\text{dc}}, n_{\text{R}})$  and the resultant pumping current  $I_P = (n_{\text{dc}} - n_{\text{R}})ef$  are denoted in the figure. The region focused in the collision experiment is therefore inside of the red and orange dashed lines, where  $n_{\text{R}} = 1$  and 2, respectively, and  $I_P = 0$ .

The collision conditions for one-electron and two-electron RQD [the intersection point of the black dashed lines in Figs. 4(a) and 5(a), respectively] are indicated by stars in Fig. 6. In the case of the one-electron RQD, it locates between the left and middle ejection lines. In this condition, only one electron can be trapped in the RQD. When there are two electrons in the RQD, one of the two electrons can be ejected to the drain, which corresponds to Fig. 4(e). In the case of the two-electron RQD, it locates between the middle and right ejection lines. In this condition, two electrons can be trapped in the RQD. When there are three electrons in the RQD, one of the three electrons can be ejected to the drain, which corresponds to Fig. 5(e).

## APPENDIX B: ESTIMATION OF CONVERSION FACTORS

To estimate the energy of the electrons, we must determine factors for converting  $V_{\text{inj}}$  ( $V_{\text{det}}$ ) into an energy value. First, let us focus on the conversion from the applied voltage into the barrier height ( $\alpha_{\text{injB}}$  and  $\alpha_{\text{detB}}$ ). Figure 7(a) shows the current flowing through the injection (detection) barrier as a function of  $V_{\text{inj}}$  ( $V_{\text{det}}$ ) at room temperature. From the fits to the data (black lines), which are  $\exp(\alpha_{\text{injB}}V_{\text{inj}}/kT + A)$  and  $\exp(\alpha_{\text{detB}}V_{\text{det}}/kT + A)$ , where  $k$  is the Boltzmann constant,  $T$  is temperature, and  $A$  is a constant, we obtain  $\alpha_{\text{injB}} = 0.41$  eV/V and  $\alpha_{\text{detB}} = 0.40$  eV/V.

Next, let us consider the cross-coupling.  $V_{\text{inj}}$  ( $V_{\text{det}}$ ) slightly changes the detection (injection) barrier. Figure 7(b) shows  $I_P$  as a function of  $V_{\text{inj}}$  and  $V_{\text{det}}$  at room temperature. The slopes  $S_{\text{injB}}$  and  $S_{\text{detB}}$  of the linear fits to the red line indicating a current level of 200 pA can be used to determine the cross-coupling from  $V_{\text{det}}$  to the injection barrier  $\alpha_{\text{det-injB}} = \alpha_{\text{injB}}/S_{\text{injB}} = 0.034$  eV/V and from  $V_{\text{inj}}$  to the detection barrier  $\alpha_{\text{inj-detB}} = \alpha_{\text{detB}}S_{\text{detB}} = 0.034$  eV/V.

Now, let us estimate the charging energy  $E_C$  of the RQD when an SE captured by the RQD is ejected to the drain. Figure 8(a) shows  $I_P$  as a function of  $V_{\text{inj}}$  and  $V_{\text{det}}$  when only the RQD pump is operated at 30 K. Current steps related to the ejection stage appear at the black dashed line in Fig. 8(a) as shown in Fig. 8(b). At this high temperature, the ejection is dominated by a thermal hopping and an equation for the current steps can be formulated as follows [5]:

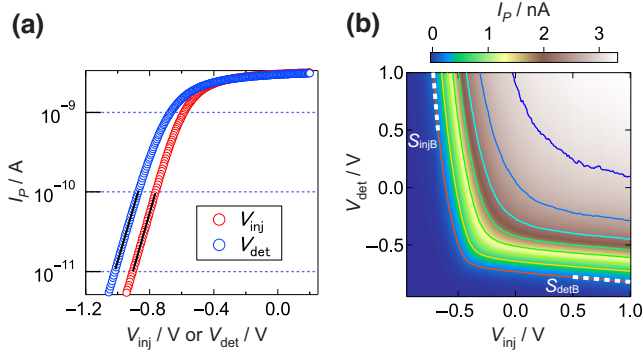


FIG. 7. (a) dc current as a function of  $V_{\text{inj}}$  ( $V_{\text{det}}$ ) at room temperature (295 K), where  $V_{\text{UG}} = 1.2$  V,  $V_{\text{inj}} = 1$  V ( $V_{\text{det}} = 1$  V),  $V_{\text{ent}} = 1$  V, and  $V_s = 1$  mV. The black lines are linear fits to  $\ln(I_P)$ . (b) dc current as a function of  $V_{\text{inj}}$  and  $V_{\text{det}}$  at room temperature (295 K), where  $V_{\text{UG}} = 1.2$  V,  $V_{\text{ent}} = 1$  V, and  $V_s = 1$  mV. The current level of the contour lines are from 200 pA (red line) to 3 nA (blue line) in steps of 400 pA. The white lines are linear fits to the red contour line. The slopes are  $S_{\text{injB}} = -12$  and  $S_{\text{detB}} = -0.084$  for the injection and detection barrier, respectively.

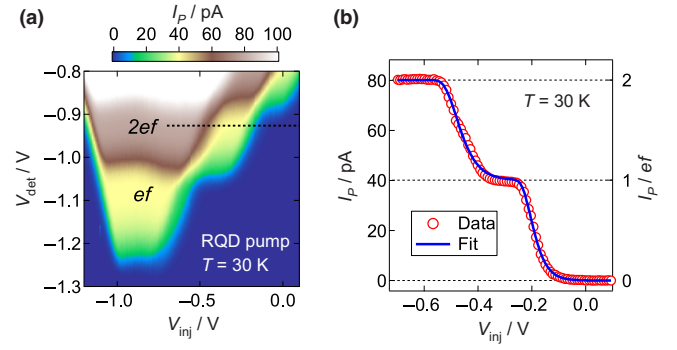


FIG. 8. (a)  $I_P$  as a function of  $V_{\text{inj}}$  and  $V_{\text{det}}$  at  $f = 250$  MHz and  $T = 30$  K, where  $V_{\text{upper}} = 1.2$  V,  $V_{\text{ent}} = 1$  V, and  $V_s = 0$  V. The high-frequency signal is only applied to  $G_{\text{inj}}$  with an amplitude  $A_{\text{inj}} = 0.3$  V. (b)  $I_P$  (red circles) as a function of  $V_{\text{inj}}$  at  $f = 250$  MHz and  $T = 30$  K, where  $V_{\text{upper}} = 1.2$  V,  $V_{\text{det}} = -0.925$  V,  $V_{\text{ent}} = 1$  V,  $V_s = 0$  V, and  $A_{\text{ent}} = 0.3$  V, corresponding to the black dashed line in (a). The blue curve is a fit to the data using Eq. (B1). The fit yields  $\alpha_1^{\text{inj}} = 0.079$  eV/V,  $\alpha_2^{\text{inj}} = 0.058$  eV/V,  $V_1 = -0.20$  V, and  $V_2 = -0.48$  V.

$$I = 2 - \sum_{n=1}^2 \exp \left[ - \exp \left\{ - \frac{\alpha_n^{\text{inj}} (V_{\text{inj}} - V_n)}{kT} \right\} \right], \quad (\text{B1})$$

where  $V_n$  is the threshold voltage of the  $n$ th plateau,  $\alpha_n^{\text{inj}}$  is equal to  $\alpha_{\text{inj-RQD}} - \alpha_{\text{inj-detB}}$  for the  $n$ th plateau, and  $\alpha_{\text{inj-RQD}}$  is the conversion factor from  $V_{\text{inj}}$  to the RQD energy. A fit to the data using this equation is shown as the blue curve in Fig. 8(b). The fit gives  $\alpha_1^{\text{inj}} \neq \alpha_2^{\text{inj}}$ , probably due to potential fluctuation. As a crude estimate, we computed the average of the two:  $\bar{\alpha}_{\text{inj}} = (\alpha_1^{\text{inj}} + \alpha_2^{\text{inj}})/2 = 0.069$  eV/V, which leads to  $E_C = \bar{\alpha}_{\text{inj}}(V_1 - V_2) = 19$  meV. This value is consistent with those for previous devices [5,46,47]. In addition,  $\alpha_{\text{inj-RQD}} = \bar{\alpha}_{\text{inj}} + \alpha_{\text{inj-detB}} = 0.10$  eV/V. Furthermore, from the slope  $S = 1.16$  of  $V_{\text{tilt}}$  [see Fig. 4(a)], we determined the conversion factor from  $V_{\text{det}}$  to the RQD ( $\alpha_{\text{det-RQD}}$ ), i.e.,  $\alpha_{\text{det-RQD}} = \alpha_{\text{detB}} - \bar{\alpha}_{\text{inj}}/S = 0.34$  eV/V [5]. All of the conversion factors are summarized in Table I. They indicate that the gate-to-barrier couplings are symmetric for the two gates and the position of the RQD is close to the detection barrier, which is consistent with the previous estimation for a different device [5].

TABLE I. Summary of the conversion factors and charging energy.

$\alpha_{\text{injB}}$	0.41 eV/V	$\alpha_{\text{inj-RQD}}$	0.10 eV/V
$\alpha_{\text{detB}}$	0.40 eV/V	$\alpha_{\text{det-RQD}}$	0.34 eV/V
$\alpha_{\text{inj-detB}}$	0.034 eV/V	$E_C$	19 meV
$\alpha_{\text{det-injB}}$	0.034 eV/V	...	...

## APPENDIX C: COLLISION PUMP MAPS

To understand pump maps in the case of the collision experiments, it is valuable to investigate them with changing  $A_{inj}$  and  $A_s$  in small steps (Fig. 9). Figure 9(a) has the same conditions as those in Fig. 5(a) except for  $V_{ent} = -0.5$  V. Figures 9(c) and 9(j) have the same conditions as those in Figs. 4(a) and 3(a), respectively.

First, we focus on the  $A_s$  dependence [Figs. 9(a)–9(e)]. In terms of the RQD pumping operation [Figs. 1(c)–1(e)], increasing  $A_s$  lowers the Fermi level in the source. The loading probability from the source to RQD in the loading stage is reduced because the height of the injection barrier [not depicted in Fig. 1(c)] relative to the source becomes high. The injection barrier is lowered to compensate this effect, leading to a movement of the loading line to the positive  $V_{inj}$  direction. From Fig. 9(a) to 9(e), the purple loading line moves in this direction. In the dynamic capture stage [Fig. 1(d)], the injection barrier height is lowered at the moment when the electrochemical potential of an SE in the RQD crosses the Fermi level. This leads to an increase in a probability of an escape of the SE back to the source. Thus, a more positive  $V_{det}$  is necessary to capture the SE by lowering the RQD potential, indicating a movement of the dynamic capture lines in the positive  $V_{det}$  direction. This movement can be seen in black dynamic capture lines from Fig. 9(a) to 9(e). In contrast to these two process, the height of the detection barrier relative to the RQD potential at the ejection stage [Fig. 1(e)] should be almost unchanged by changing the source voltage, implying no change in the

ejection lines. This is confirmed by the fact that the light-blue ejection lines do not move. Since the experimental observation is consistent with the expectation of the normal pump map behavior even when there is an additional current due to the LQD pumping (explained below), we conclude that the purple, black, and light-blue lines correspond to the pump map for the RQD pump, i.e., the same as Fig. 2(c). This fact indicates that the number of SEs after the RQD pump operation with voltage conditions inside the red (orange) dashed line in Fig. 4(a) [Fig. 5(a)] is one (two) as shown in Fig. 6.

Additional features indicated by red lines in Fig. 9 should be related to the LQD pumping [Figs. 1(f)–1(h)]. Similar to the case of the RQD pumping, the detection barrier is not affected by the effect of  $A_s$  in the LQD pumping. Since the red line rising to the right does not move from Fig. 9(a) to 9(e) and it is parallel to the light-blue ejection lines of the RQD pump map, it is the boundary that indicates that the detection barrier prevents the transmission of hot SEs injected from the LQD into RQD. Increasing  $A_s$  raises the Fermi level in the source during the LQD pumping. Opposite to the case of the dynamic capture stage of the RQD pumping, the electrochemical potential of an SE in the LQD should be raised to compensate the effect of  $A_s$  by applying a more negative  $V_{inj}$ . As expected, the vertical red lines moves in the negative  $V_{inj}$  direction from Figs. 9(a) to 9(e). Of note, there is no clear discrete shift of all the boundaries, indicating almost independent operations of the LQD and RQD pumps.

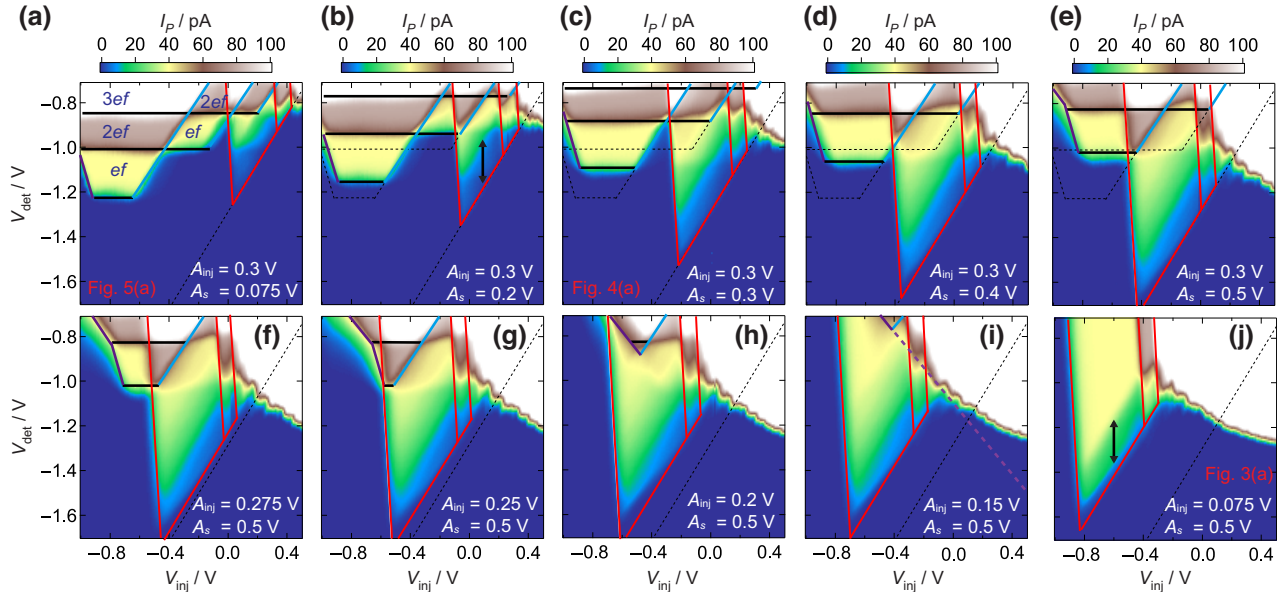


FIG. 9.  $I_p$  as a function of  $V_{inj}$  and  $V_{det}$  with the pulse sequence shown in Fig. 1(b), where  $V_{upper} = 1.2$  V,  $V_{ent} = -0.5$  V,  $V_s = 0$  V, and  $A_{ent} = 0.3$  V.  $(A_{inj}, A_s)$  is changed in each panel: (0.3 V, 0.075 V) in (a), (0.3 V, 0.2 V) in (b), (0.3 V, 0.3 V) in (c), (0.3 V, 0.4 V) in (d), (0.3 V, 0.5 V) in (e), (0.275 V, 0.5 V) in (f), (0.25 V, 0.5 V) in (g), (0.2 V, 0.5 V) in (h), (0.15 V, 0.5 V) in (i), and (0.075 V, 0.5 V) in (j). Black dashed lines are copies of the boundaries in (a).

As can be seen in Figs. 9(a)–9(e), the change in  $A_s$  is mainly affected to the dynamic capture condition. The number of SEs injected from the LQD and that confined in the RQD during the RQD pumping are mainly tuned in each dynamic capture stage. Therefore, we can change the experimental condition from an SE injection from the LQD into the one-electron RQD to that into the two-electron RQD by changing  $A_s$ .

Next, we focus on the  $A_{\text{inj}}$  dependence [Figs. 9(f)–9(j)]. With decreasing  $A_{\text{inj}}$ , the RQD pump map becomes small and eventually disappears in this voltage region. For the LQD pump, more negative  $V_{\text{inj}}$  compensates the decrease in  $A_{\text{inj}}$ , leading to the movement of the red lines in the negative  $V_{\text{inj}}$  direction. Therefore, we conclude that Fig. 9(j), corresponding to the Fig. 3(a), is operation of the LQD pump without an additional pumping current generated during the RQD pumping operation [Figs. 1(c)–1(e)]. This point is also confirmed by the observation of the normal pump map of the LQD [Fig. 3(b)]. We should again focus on the number of SEs trapped in the RQD in the condition of Fig. 9. As explained in Appendix A, the loading of electrons from the source to the RQD is prohibited in the left side of the loading line. This also indicates that the number of the RQD is not always reset. When an SE injected from the LQD is trapped by the RQD, it could remain captured by the RQD in this region. In Figs. 9(i) and 9(j), the LQD pumping condition is located in the left side of the purple dashed loading line as shown in Fig. 9(i). Therefore, there is the possibility that the number of the SEs in the RQD is not zero. We speculate that the difference of the characteristics between Figs. 9(i) and 9(j) is related to the number of SEs in the RQD. In contrast to these cases, the collision condition [Figs. 9(a) and 9(c)] is located at the right side of the purple loading line. This indicates that the number of SEs in the RQD is reset in every cycle.

We should also note that the two-step feature shown in Fig. 3(c) also appears in the case of the collision condition as indicated black arrows in Figs. 9(b) and 9(j). As mentioned in the main text, we need further experiments to clarify the origin of this step feature as a future subject.

#### APPENDIX D: SUPPRESSION OF HOT-SE INJECTION FROM THE LQD

To suppress the hot-SE injection from the LQD in the collision condition shown in Fig. 5(b), we changed  $V_{\text{ent}}$  as shown in Fig. 10 using the operating conditions in Fig. 5(a) with fixing  $V_{\text{det}}$  to be a value of the horizontal black dashed line. The vertical blue and red dashed lines correspond to the blue and red lines in Fig. 5(b). Two parallel black dashed lines correspond to the ejection lines of the RQD pumping. The LQD pump map indicated by the purple loading, black dynamic capture, light-blue ejection lines is clearly seen at the left top region in this graph. Since

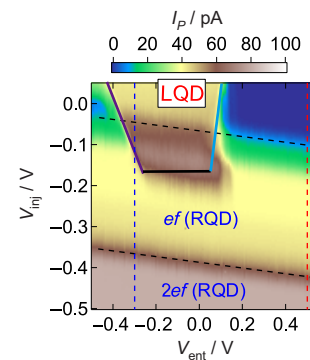


FIG. 10.  $I_p$  as a function of  $V_{\text{ent}}$  and  $V_{\text{inj}}$  with the pulse sequence shown in Fig. 1(b), where  $V_{\text{upper}} = 1.2$  V,  $V_{\text{det}} = -0.91$  V,  $V_s = 0$  V,  $A_{\text{ent}} = 0.3$  V,  $A_{\text{inj}} = 0.3$  V, and  $A_s = 0.075$  V.

the upper black dashed line is straight, it would be reasonable to compare the red and blue dashed lines with a shift extracted from the slope of the black dashed lines as performed in Fig. 5(b).

- [1] B. Kaestner and V. Kashcheyevs, Non-adiabatic quantized charge pumping with tunable-barrier quantum dots: A review of current progress, *Rep. Prog. Phys.* **78**, 103901 (2015).
- [2] J. P. Pekola, O.-P. Saira, V. F. Maisi, A. Kemppinen, M. Möttönen, Y. A. Pashkin, and D. V. Averin, Single-electron current sources: Toward a refined definition of the ampere, *Rev. Mod. Phys.* **85**, 1421 (2013).
- [3] S. P. Giblin, A. Fujiwara, G. Yamahata, M.-H. Bae, N. Kim, A. Rossi, M. Möttönen, and M. Kataoka, Evidence for universality of tunable-barrier electron pumps, *Metrologia* **56**, 044004 (2019).
- [4] C. Bäuerle, D. C. Glattli, T. Meunier, F. Portier, P. Roche, P. Roulleau, S. Takada, and X. Waintal, Coherent control of single electrons: A review of current progress, *Rep. Prog. Phys.* **81**, 056503 (2018).
- [5] G. Yamahata, S. Ryu, N. Johnson, H.-S. Sim, A. Fujiwara, and M. Kataoka, Picosecond coherent electron motion in a silicon single-electron source, *Nat. Nanotechnol.* **14**, 1019 (2019).
- [6] N. Johnson, J. D. Fletcher, D. A. Humphreys, P. See, J. P. Griffiths, G. A. C. Jones, I. Farrer, D. A. Ritchie, M. Pepper, T. J. B. M. Janssen, and M. Kataoka, Ultrafast voltage sampling using single-electron wavepackets, *Appl. Phys. Lett.* **110**, 102105 (2017).
- [7] N. Ubbelohde, F. Hohls, V. Kashcheyevs, T. Wagner, L. Fricke, B. Kästner, K. Pierz, H. W. Schumacher, and R. J. Haug, Partitioning of on-demand electron pairs, *Nat. Nanotechnol.* **10**, 46 (2015).
- [8] J. D. Fletcher, N. Johnson, E. Locane, P. See, J. P. Griffiths, I. Farrer, D. A. Ritchie, P. W. Brouwer, V. Kashcheyevs, and M. Kataoka, Continuous-variable tomography of solitary electrons, *Nat. Commun.* **10**, 5298 (2019).
- [9] G. Yamahata, S. P. Giblin, M. Kataoka, T. Karasawa, and A. Fujiwara, Gigahertz single-electron pumping in silicon

- with an accuracy better than 9.2 parts in  $10^7$ , *Appl. Phys. Lett.* **109**, 013101 (2016).
- [10] R. Zhao, A. Rossi, S. P. Giblin, J. D. Fletcher, F. E. Hudson, M. Möttönen, M. Kataoka, and A. S. Dzurak, Thermal-error regime in high-accuracy gigahertz single-electron pumping, *Phys. Rev. Appl.* **8**, 044021 (2017).
- [11] S. P. Giblin, E. Mykkänen, A. Kemppinen, P. Immonen, A. Manninen, M. Jenei, M. Möttönen, G. Yamahata, A. Fujiwara, and M. Kataoka, Realisation of a quantum current standard at liquid helium temperature with sub-ppm reproducibility, *Metrologia* **57**, 025013 (2020).
- [12] A. Fujiwara, G. Yamahata, and N. Johnson, in *Conference on Precision Electromagnetic Measurements (CPEM 2022)* (2022), <https://ieeexplore.ieee.org/xpl/conhome/1000590/all-proceedings>.
- [13] V. Kashcheyevs and B. Kaestner, Universal decay cascade model for dynamic quantum dot initialization, *Phys. Rev. Lett.* **104**, 186805 (2010).
- [14] G. Yamahata, N. Johnson, and A. Fujiwara, Understanding the mechanism of tunable-barrier single-electron pumping: Mechanism crossover and optimal accuracy, *Phys. Rev. B* **103**, 245306 (2021).
- [15] H. Edlbauer, *et al.*, Semiconductor-based electron flying qubits: Review on recent progress accelerated by numerical modelling, *EPJ Quantum Technol.* **9**, 21 (2022).
- [16] M. Yamamoto, S. Takada, C. Bäuerle, K. Watanabe, A. D. Wieck, and S. Tarucha, Electrical control of a solid-state flying qubit, *Nat. Nanotechnol.* **7**, 247 (2012).
- [17] S. Takada, H. Edlbauer, H. V. Lepage, J. Wang, P.-A. Mortemousque, G. Georgiou, C. H. W. Barnes, C. J. B. Ford, M. Yuan, P. V. Santos, X. Waintal, A. Ludwig, A. D. Wieck, M. Urdampilleta, T. Meunier, and C. Bäuerle, Sound-driven single-electron transfer in a circuit of coupled quantum rails, *Nat. Commun.* **10**, 4557 (2019).
- [18] R. Ito, S. Takada, A. Ludwig, A. D. Wieck, S. Tarucha, and M. Yamamoto, Coherent beam splitting of flying electrons driven by a surface acoustic wave, *Phys. Rev. Lett.* **126**, 070501 (2021).
- [19] T. Shimizu, J. Ohe, A. Endo, T. Nakamura, and S. Katsumoto, Half-mirror for electrons in quantum Hall copropagating edge channels in a Mach-Zehnder interferometer, *Phys. Rev. Appl.* **19**, 034085 (2023).
- [20] P. Kok, W. J. Munro, K. Nemoto, T. C. Ralph, J. P. Dowling, and G. J. Milburn, Linear optical quantum computing with photonic qubits, *Rev. Mod. Phys.* **79**, 135 (2007).
- [21] J. L. O'Brien, A. Furusawa, and J. Vučković, Photonic quantum technologies, *Nat. Photonics* **3**, 687 (2009).
- [22] R. Ionicioiu, G. Amaratunga, and F. Udrea, Quantum computation with ballistic electrons, *Int. J. Mod. Phys. B* **15**, 125 (2001).
- [23] J. D. Fletcher, W. Park, S. Ryu, P. See, J. P. Griffiths, G. A. C. Jones, I. Farrer, D. A. Ritchie, H.-S. Sim, and M. Kataoka, Time-resolved Coulomb collision of single electrons, *Nat. Nanotechnol.* **18**, 727 (2023).
- [24] N. Ubbelohde, L. Freise, E. Pavlovskaya, P. G. Silvestrov, P. Recher, M. Kokainis, G. Barinovsky, F. Hohls, T. Weimann, K. Pierz, and V. Kashcheyevs, Two electrons interacting at a mesoscopic beam splitter, *Nat. Nanotechnol.* **18**, 733 (2023).
- [25] J. Wang, H. Edlbauer, A. Richard, S. Ota, W. Park, J. Shim, A. Ludwig, A. D. Wieck, H.-S. Sim, M. Urdampilleta, T. Meunier, T. Kodera, N.-H. Kaneko, H. Sellier, X. Waintal, S. Takada, and C. Bäuerle, Coulomb-mediated antibunching of an electron pair surfing on sound, *Nat. Nanotechnol.* **18**, 721 (2023).
- [26] L. Bellentani, P. Bordone, X. Oriols, and A. Bertoni, Coulomb and exchange interaction effects on the exact two-electron dynamics in the Hong-Ou-Mandel interferometer based on Hall edge states, *Phys. Rev. B* **99**, 245415 (2019).
- [27] S. Ryu and H.-S. Sim, Partition of two interacting electrons by a potential barrier, *Phys. Rev. Lett.* **129**, 166801 (2022).
- [28] E. Pavlovskaya, P. G. Silvestrov, P. Recher, G. Barinovsky, and V. Kashcheyevs, Collision of two interacting electrons on a mesoscopic beamsplitter: Exact solution in the classical limit, *Phys. Rev. B* **107**, 165304 (2023).
- [29] T. Sakamoto, H. Kawaura, T. Baba, and T. Iizuka, Characteristic length of hot-electron transport in silicon metal-oxide-semiconductor field-effect transistors, *Appl. Phys. Lett.* **76**, 2618 (2000).
- [30] H. Firdaus, T. Watanabe, M. Hori, D. Moraru, Y. Takahashi, A. Fujiwara, and Y. Ono, Electron aspirator using electron-electron scattering in nanoscale silicon, *Nat. Commun.* **9**, 4813 (2018).
- [31] A. Fujiwara, K. Nishiguchi, and Y. Ono, Nanoampere charge pump by single-electron ratchet using silicon nanowire metal-oxide-semiconductor field-effect transistor, *Appl. Phys. Lett.* **92**, 042102 (2008).
- [32] T. Ota, S. Akiyama, M. Hashisaka, K. Muraki, and T. Fujisawa, Spectroscopic study on hot-electron transport in a quantum Hall edge channel, *Phys. Rev. B* **99**, 085310 (2019).
- [33] J. D. Fletcher, P. See, H. Howe, M. Pepper, S. P. Giblin, J. P. Griffiths, G. A. C. Jones, I. Farrer, D. A. Ritchie, T. J. B. M. Janssen, and M. Kataoka, Clock-controlled emission of single-electron wave packets in a solid-state circuit, *Phys. Rev. Lett.* **111**, 216807 (2013).
- [34] L. Freise, T. Gerster, D. Reifert, T. Weimann, K. Pierz, F. Hohls, and N. Ubbelohde, Trapping and counting ballistic nonequilibrium electrons, *Phys. Rev. Lett.* **124**, 127701 (2020).
- [35] C. Hamaguchi, *Basic Semiconductor Physics* (Springer International Publishing, Cham, 2017), 3rd edn.
- [36] R. Brunetti, C. Jacoboni, F. Nava, L. Reggiani, G. Bosman, and R. J. J. Zijlstra, Diffusion coefficient of electrons in silicon, *J. Appl. Phys.* **52**, 6713 (1981).
- [37] S. Takagi, J. L. Hoyt, J. J. Welser, and J. F. Gibbons, Comparative study of phonon-limited mobility of two-dimensional electrons in strained and unstrained Si metal-oxide-semiconductor field-effect transistors, *J. Appl. Phys.* **80**, 1567 (1996).
- [38] C. H. Yang, R. C. C. Leon, J. C. C. Hwang, A. Saraiva, T. Tantt, W. Huang, J. C. Lemyre, K. W. Chan, K. Y. Tan, F. E. Hudson, K. M. Itoh, A. Morello, M. Pioro-Ladrière, A. Laucht, and A. S. Dzurak, Operation of a silicon quantum processor unit cell above one kelvin, *Nature* **580**, 350 (2020).
- [39] L. Petit, M. Russ, G. H. G. J. Eenink, W. I. L. Lawrie, J. S. Clarke, L. M. K. Vandersypen, and M. Veldhorst, Design

- and integration of single-qubit rotations and two-qubit gates in silicon above one kelvin, *Commun. Mater.* **3**, 82 (2022).
- [40] A. Noiri, K. Takeda, T. Nakajima, T. Kobayashi, A. Sammak, G. Scappucci, and S. Tarucha, Fast universal quantum gate above the fault-tolerance threshold in silicon, *Nature* **601**, 338 (2022).
- [41] X. Xue, M. Russ, N. Samkharadze, B. Undseth, A. Sammak, G. Scappucci, and L. M. K. Vandersypen, Quantum logic with spin qubits crossing the surface code threshold, *Nature* **601**, 343 (2022).
- [42] K. Takeda, A. Noiri, T. Nakajima, T. Kobayashi, and S. Tarucha, Quantum error correction with silicon spin qubits, *Nature* **608**, 682 (2022).
- [43] S. G. J. Philips, M. T. Maądzik, S. V. Amitonov, S. L. de Snoo, M. Russ, N. Kalhor, C. Volk, W. I. L. Lawrie, D. Brousse, L. Tryputen, B. P. Wuetz, A. Sammak, M. Veldhorst, G. Scappucci, and L. M. K. Vandersypen, Universal control of a six-qubit quantum processor in silicon, *Nature* **609**, 919 (2022).
- [44] B. Bertrand, S. Hermelin, S. Takada, M. Yamamoto, S. Tarucha, A. Ludwig, A. D. Wieck, C. Bäuerle, and T. Meunier, Fast spin information transfer between distant quantum dots using individual electrons, *Nat. Nanotechnol.* **11**, 672 (2016).
- [45] B. Jadot, P.-A. Mortemousque, E. Chanrion, V. Thiney, A. Ludwig, A. D. Wieck, M. Urdampilleta, C. Bäuerle, and T. Meunier, Distant spin entanglement via fast and coherent electron shuttling, *Nat. Nanotechnol.* **16**, 570 (2021).
- [46] N. Johnson, G. Yamahata, and A. Fujiwara, Measurement of the curvature and height of the potential barrier for a dynamic quantum dot, *Appl. Phys. Lett.* **115**, 162103 (2019).
- [47] G. Yamahata, K. Nishiguchi, and A. Fujiwara, Accuracy evaluation of single-electron shuttle transfer in Si nanowire metal-oxide-semiconductor field-effect transistors, *Appl. Phys. Lett.* **98**, 222104 (2011).